

ARTICLE TYPE

Accurate quantification of blood flow wall shear stress using simulation-based imaging: a synthetic, comparative study

Charles J. Naudet¹ | Johannes Töger² | Matthew J. Zahr*¹

¹Department of Aerospace and Mechanical Engineering, University of Notre Dame, Indiana, USA

²Department of Clinical Sciences Lund, Clinical Physiology, Lund University, Skåne University Hospital, Lund, Sweden

Correspondence

*Matthew J. Zahr, 300B Cushing Hall, Notre Dame, IN 46656. Email: mzahr@nd.edu

Abstract

Simulation-based imaging (SBI) is a blood flow imaging technique that optimally fits a computational fluid dynamics (CFD) simulation to low-resolution, noisy magnetic resonance (MR) flow data to produce a high-resolution velocity field. In this work, we study the effectivity of SBI in predicting wall shear stress (WSS) relative to standard magnetic resonance imaging (MRI) postprocessing techniques using two synthetic numerical experiments: flow through an idealized, two-dimensional stenotic vessel and a model of an adult aorta. In particular, we study the sensitivity of these two approaches with respect to the Reynolds number of the underlying flow, the resolution of the MRI data, and the noise in the MRI data. We found that the SBI WSS reconstruction: 1) is insensitive to Reynolds number over the range considered ($Re \leq 1000$), 2) improves as the amount of MRI data increases and provides accurate reconstructions with as little as three MRI voxels per diameter, and 3) degrades linearly as the noise in the data increases with a slope determined by the resolution of the MRI data. We also consider the sensitivity of SBI to the resolution of the CFD mesh and found there is flexibility in the mesh used for SBI, although the WSS reconstruction becomes more sensitive to other parameters, particularly the resolution of the MRI data, for coarser meshes. This indicates a fundamental trade-off between scan time (i.e., MRI data quality and resolution) and reconstruction time using SBI, which is inherently different than the trade-off between scan time and reconstruction quality observed in standard MRI postprocessing techniques.

KEYWORDS:

Simulation-based imaging, magnetic resonance imaging, wall shear stress, congenital heart disease

1 | BACKGROUND

Magnetic resonance imaging (MRI) is a powerful method to investigate cardiovascular physiology. High-resolution *in vivo* images can help understand patient-specific blood flow and provide important quantitative biomarkers such as wall shear stress (WSS). However, these methods are limited by a fundamental trade-off between scan time, resolution, and noise^{1,2}, which limits their utility for applications that demand very high-resolution images such as infants and children with congenital heart disease³. This is further complicated when estimates of biomarkers must be extracted from these flow images with poorly resolved features. This motivates the need for imaging methods that can use sparse, noisy data to provide sufficiently high-resolution reconstructions that can be used to accurately compute quantitative biomarkers.

Recent advances in compressed sensing^{4,5,6,7} and machine learning^{8,9} have been used to enhance MRI-based flow reconstructions, leading to improved image quality and reduced scan times. Neural networks have proven effective in taking sparse or missing data in k-space and accurately reconstructing them into natural images. Machine learning approaches are valuable, but face drawbacks of high training cost and not being patient-specific. Several simulation-based imaging (SBI) methods^{10,11,12,13,14,15,16,17,18} exist that match a computational fluid dynamics (CFD) simulation to magnetic resonance (MR) flow data by optimizing free parameters of the CFD simulation (usually boundary and initial conditions), use a metric to measure the difference between CFD and MR flow imaging, and update the free parameters to minimize the cost function via their own strategy. The method used in this work¹⁷ uses a high-order CFD discretization, efficient adjoint-based PDE-constrained optimization, and a novel objective function that mimics the point-spread function of MRI scanners. This method was shown to effectively reconstruct very high-resolution velocity fields from limited MRI data and match ground truth values for both a controlled water tank experiment and an *in vivo* clinical application. However, the quality to which the method predicts quantitative biomarkers has not been considered to date.

In this paper, we study the accuracy to which the SBI approach of¹⁷ predicts the WSS distribution relative to standard MRI postprocessing approaches using two synthetic numerical experiments. We focus on WSS because it is known to correlate to atherosclerosis, the formation and rupture aneurysms, as well as numerous congenital heart diseases^{19,20,21,22,23,24,25,26,27,28,29}. Furthermore, it has proven difficult to estimate directly using standard MRI postprocessing techniques^{30,31,32} because WSS requires accurate estimation of the velocity gradient that can be difficult using only piecewise constant voxel data. Current methods for postprocessing MR flow data to obtain quantities of interest, e.g., phase-contrast (PC) MRI velocity mapping, Fourier velocity encoding (FVE), and intravoxel velocity standard deviation mapping^{33,34,35}, can be unreliable.

We study the impact of the Reynolds number of the underlying flow and the resolution and noise of the MRI data to understand the sensitivity of each method with respect to these critical parameters. Noise is a critical source of error for *in vivo* imaging and extraction of biomarkers³⁶ and becomes increasingly problematic as the resolution of the MRI grid increases or if faster scans are required, e.g. for sedated children or to reduce costs of health care. On the other hand, the resolution of the MRI data can lead to higher resolution images and more accurate biomarker computations; however, it is usually accompanied with increased noise and requires longer scans. The Reynolds number is studied because it has been observed that the accuracy of the WSS computed directly from MRI data decreases as the Reynolds number of the flow increases³⁴. Furthermore, we study the impact of the resolution of the CFD mesh used in SBI because this determines the overall cost of the reconstruction.

2 | METHODS

Two synthetic numerical experiments were conducted to compare the accuracy of MRI methods with SBI in measuring wall shear stress. To perform comprehensive studies, SBI was simplified for use in two-dimensional, time-independent problems, instead of three-dimensional, unsteady problems as in our previous study¹⁷. The experiments are synthetic in the sense that no *in vivo* MRI flow data or geometries were used; synthetic data was constructed to be representative of a realistic situation and consistent with *in vivo* measurements to the extent possible, e.g., regarding noise levels, MRI resolution, and extraction of MRI data from a velocity field. The synthetic experiments allow for a highly controlled study with a known reference (“truth”) flow so the impact of various parameters, e.g., Reynolds number, noise, MRI grid resolution, on WSS reconstruction accuracy can be isolated and identified. The remainder of this section will describe the numerical experiments in detail. Section 2.1 introduces the setup of the synthetic experiments, Section 2.2 details the creation of synthetic MRI data and WSS reconstruction, and Section 2.3 reviews the SBI method and corresponding WSS computation.

2.1 | Synthetic experiments

We use two synthetic experiments to investigate the accuracy of WSS measurements from SBI relative to standard MRI methods: 1) flow through an idealized stenotic vessel and 2) flow through an idealized aorta with a coarctation. The geometry of the stenotic vessel with 60% grade is the set $\Omega \subset \mathbb{R}^d$ ($d = 2$ in this work; formulas not pertaining to domain geometries hold for general d), defined as

$$\Omega := \{(x, \pm y(x)) \mid x \in [0, 6]\}, \quad y : x \mapsto B_0 - \frac{A}{\sqrt{2\pi\sigma^2}} \exp\left(-\frac{(x-c)^2}{2\sigma^2}\right) \quad (1)$$

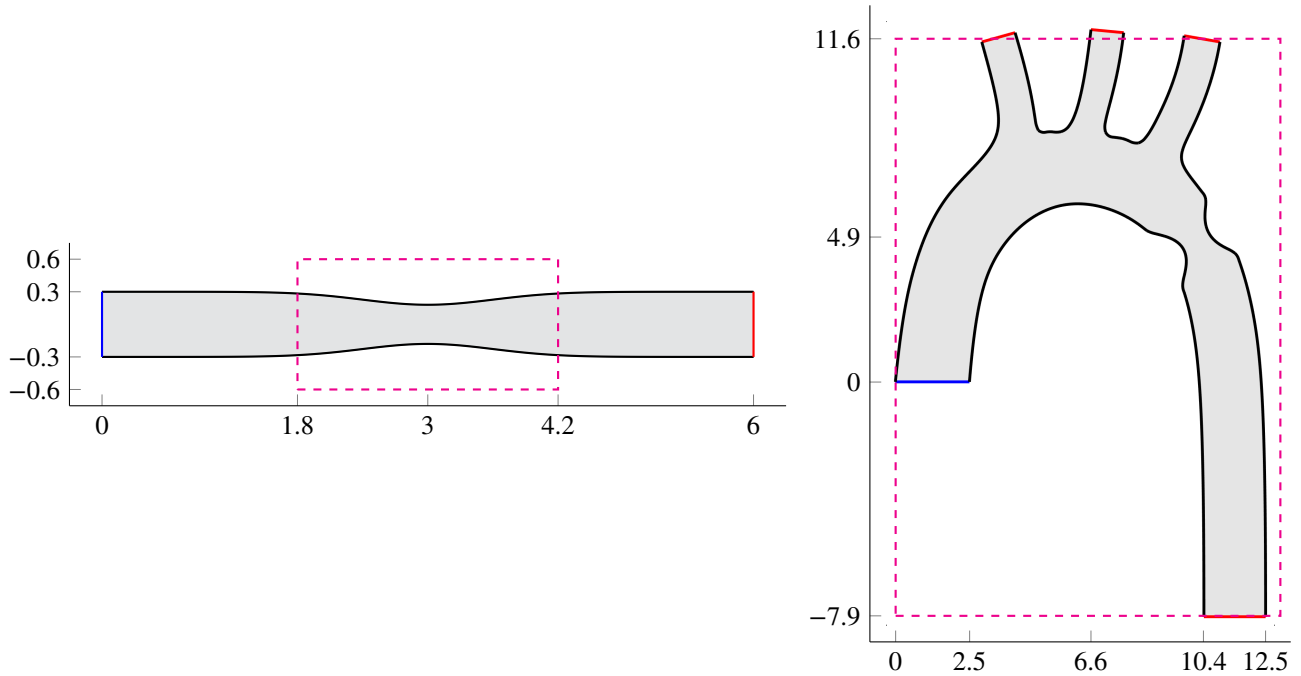


FIGURE 1 Idealized stenotic vessel with 60% grade (*left*) and coarctated aorta with 40% grade (*right*) geometry Ω used for numerical experiments with boundaries: $\partial\Omega_w$ (—), $\partial\Omega_{in}$ (—), $\partial\Omega_{out}$ (—). The MRI scan region for each geometry is indicated with (---). Units: cm.

where $B_0 = 0.3$ cm, $c = 3$ cm, $\sigma = 0.6$ cm, $A = 0.18$ cm² (Figure 1). The geometry of the coarctated aorta (40% grade) is shown in Figure 1. In practice, these geometries would be obtained from MRI scans; however, we chose to explicitly define the geometry to ensure a controlled setting in which to study WSS reconstruction. Most of the studies in this work are conducted using the vessel due to its simplicity; the aorta is used to confirm our findings on a more realistic geometry.

The blood flow is modeled as an incompressible, Newtonian fluid governed by the Navier-Stokes equations

$$\frac{\partial v}{\partial t} + (v \cdot \nabla)v - \nu \nabla^2 v + \frac{1}{\rho_0} \nabla P = 0, \quad \nabla \cdot v = 0 \quad \text{in } \Omega, \quad (2)$$

where $\rho_0 \in \mathbb{R}_{>0}$ is the density of the fluid, $\nu \in \mathbb{R}_{>0}$ is the kinematic viscosity of the fluid, and $v : \Omega \rightarrow \mathbb{R}^d$ and $P : \Omega \rightarrow \mathbb{R}_{>0}$ are the velocity and pressure, respectively, of the fluid implicitly defined as the solution of (2). In this work, we assume the fluid is blood and take the material properties to be $\rho_0 = 1060$ kg/m³³⁷ and $\nu = 2.83 \times 10^{-6}$ m²/s³⁸ for both test cases. We consider the case where the flow has reached a steady state and the time derivative, $\frac{\partial v}{\partial t}$, vanishes. Boundary conditions for the boundaries identified in Figure 1 are

$$v = 0 \quad \text{on } \partial\Omega_w, \quad v = v_{in} \quad \text{on } \partial\Omega_{in}, \quad \sigma \cdot n = 0 \quad \text{on } \partial\Omega_{out} \quad (3)$$

where $v_{in} : x \mapsto \bar{v}_{in}(B_0^2 - x_2^2)/B_0^2$ is the parabolic inlet profile with peak value $\bar{v}_{in} \in \mathbb{R}^d$ (for the stenotic vessel) and $n : \partial\Omega \rightarrow \mathbb{R}^d$ is the outward unit normal to the boundary of the domain. The rate-of-strain, $\epsilon : \Omega \rightarrow \mathbb{R}^{d \times d}$, and stress, $\sigma : \Omega \rightarrow \mathbb{R}^{d \times d}$, tensors are defined as

$$\epsilon = \frac{1}{2}(\nabla v + \nabla v^T), \quad \sigma = 2\mu\epsilon + P I_d, \quad (4)$$

where $\mu = \rho_0 \nu$ is the dynamic viscosity and I_d is the $d \times d$ identity matrix. The Reynolds number, $\text{Re} \in \mathbb{R}_{>0}$, of the flow is defined based on the full cross-sectional diameter of the geometry, $D \in \mathbb{R}_{>0}$, and the peak inlet velocity as $\text{Re} = \frac{D \|\bar{v}_{in}\|}{\nu}$. The WSS, $\sigma^{wss} : \partial\Omega \rightarrow \mathbb{R}$, the quantitative biomarker considered in this work, is defined as the magnitude of the tangential component of the surface traction³⁹

$$t = \sigma \cdot n, \quad \tau = t - (t \cdot n)n, \quad \sigma^{wss} = \|\tau\|, \quad (5)$$

where $t : \partial\Omega \rightarrow \mathbb{R}^d$ is the surface traction and $\tau : \partial\Omega \rightarrow \mathbb{R}^d$ is its tangential component.

The Navier-Stokes equations are approximated using the finite element method on an unstructured triangular mesh consisting of $\mathcal{P}^3 - \mathcal{P}^2$ Taylor-Hood elements. A linear mesh (straight-sided triangles) is generated using DistMesh⁴⁰ and the boundary edges

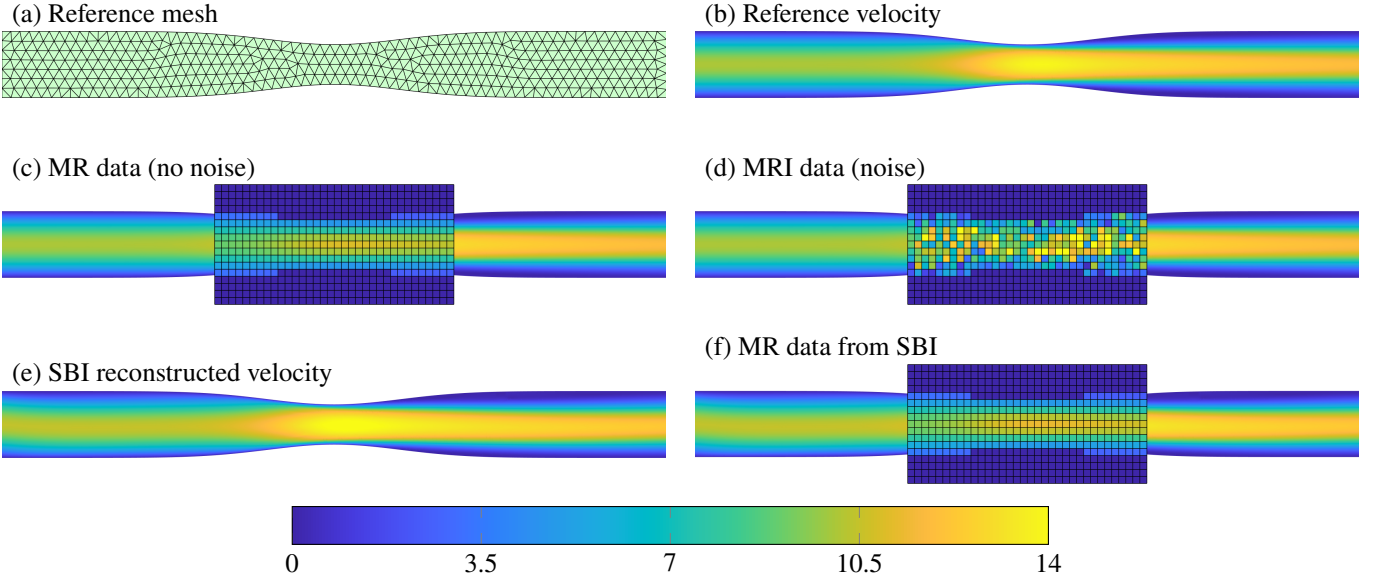


FIGURE 2 Computational mesh (a) and corresponding velocity field (b) used to define the true flow (v_h) through the stenotic vessel ($Re = 1000$). The velocity field is mapped to the MR data space ($\Xi_i(v_h)$) to produce the noise-free MRI data (c); the MRI grid contains $N = 9$ VPD. The Gaussian noise model with standard deviation equal to $\kappa = 20\%$ of the peak velocity is added to the noise-free MRI data to produce the actual MRI data (\bar{v}_i) (d). Simulation-based imaging is used to reconstruct the velocity field from the noisy MRI data, which leads to the field ($v_H(\cdot; \mu^*)$) (e) and corresponding representation in the MR data space ($\Xi_i(v_H(\cdot; \mu^*))$) (f). Colorbar: $\|v\|$ [cm/s].

are projected onto the exact geometry (and interior nodes smoothed) for a high-order representation. Let v_h denote the finite element solution of the Navier-Stokes equations. This CFD solution defines our reference or “truth” flow, e.g., corresponding to the *in vivo* flow, which is not available in practice, but essential to conduct thorough inquiries. The reference or “truth” value for WSS is computed from (5) using the finite element solution v_h ; the pointwise velocity and necessary derivatives are readily available from the finite element basis functions. The reference WSS value computed from the reference finite element solution v_h is denoted σ_h^{wss} . Figures 2 and 3 show the computational mesh and corresponding velocity field ($Re = 1000$) used to define the true flow for the stenosis and aorta test cases, respectively. The corresponding WSS (σ_h^{wss}) is shown in Figure 4 for both test cases. Synthetic MRI data is extracted from the reference solution v_h and perturbed with noise using the approach in¹⁷ (summarized in Section 2.2). In Section 3, we will use this synthetic MRI data to reconstruct the WSS using standard MRI techniques (Section 2.2) and SBI (Section 2.3) to study the accuracy and sensitivity of each approach.

2.2 | Magnetic resonance imaging

Flow MRI scans extract velocities averaged over a Cartesian grid of voxels from an *in vivo* flow. The resolution of the voxel grid determines both the resolution and noise of the velocity data^{1,2}. In blood flow imaging, the resolution is measured and reported in millimeters, but an important metric for flow accuracy is the number of voxels per diameter (VPD)⁴¹, which can range from 5-20 VPD for adults⁴² and 3-5 VPD for infants^{43,44}.

In the synthetic setting, we compute synthetic data consistent with the approach in¹⁷, specialized to the case of steady flow, i.e., a weighted integral of the true velocity field over a given voxel and its neighbors. For simplicity, we assume the voxel grid is aligned with the coordinate axes. We consider a grid consisting of N_x voxels in the x_1 -direction and N_y voxels in the x_2 -direction and let $\Delta x, \Delta y \in \mathbb{R}_{>0}$ denote the spacing of the voxel grid in the respective direction. We endow the $N = N_x N_y$ voxels with an ordering and let $(X_i, Y_i) \in \mathbb{R}^2$ denote the centroid of the i th voxel for $i = 1, \dots, N$. We leverage an abuse of notation to let N denote the resolution of the voxel grid, either stated in terms of the total number of voxels ($N_x N_y$) or the number of VPD, depending on the context. With this notation, the synthetic MR flow velocity data associated with the i th voxel, $\bar{v}_i \in \mathbb{R}^2$, is extracted from a CFD simulation as

$$\bar{v}_i := \Xi_i(v_h) + \varphi_i, \quad (6)$$

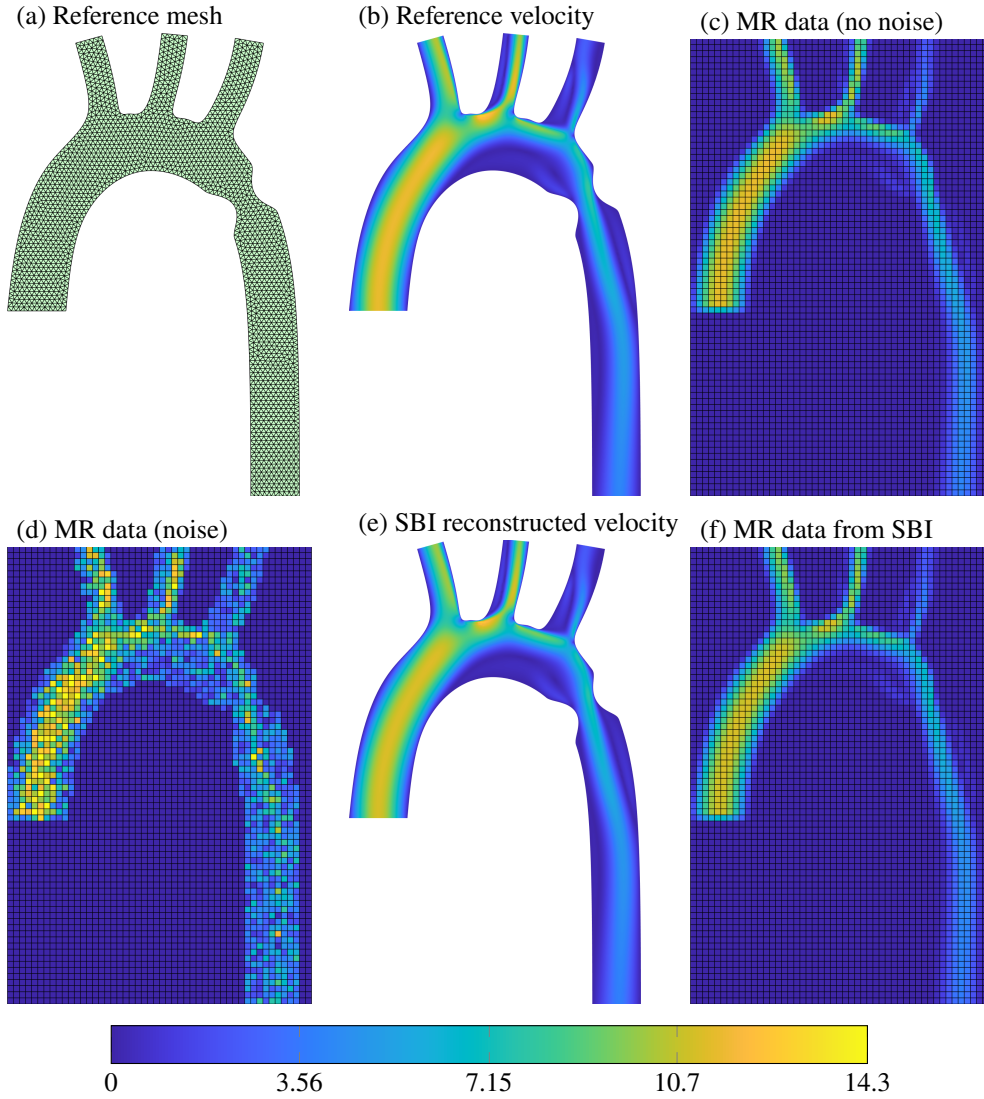


FIGURE 3 Computational mesh (a) and corresponding velocity field (b) used to define the true flow (v_h) through the aorta ($\text{Re} = 1000$). The velocity field is mapped to the MR data space ($\Xi_i(v_h)$) to produce the noise-free MRI data (c); the MRI grid contains $N = 10$ VPD. The Gaussian noise model with standard deviation equal to $\kappa = 20\%$ of the peak velocity is added to the noise-free MRI data to produce the actual MRI data (\bar{v}_i) (d). Simulation-based imaging is used to reconstruct the velocity field from the noisy MRI data, which leads to the field ($v_H(\cdot; \mu^*)$) (e) and corresponding representation in the MR data space ($\Xi_i(v_H(\cdot; \mu^*))$) (f). Colorbar: $\|v\|$ [cm/s].

where φ_i is a normally distributed random variable with mean 0 and standard deviation proportional to the peak flow velocity, i.e., $\kappa \sup_{x \in \Omega} v_h(x)$ with noise level $\kappa \in \mathbb{R}_{\geq 0}$, and $\varphi_1, \dots, \varphi_N$ are independent and identically distributed^{45,46}. Following the approach in¹⁷, the point-spread function maps a continuous velocity field to the MR data space through a weighted average of the velocity field over a given voxel as

$$\Xi_i : u \mapsto \int_{\Omega} w_i u \, dv \quad (7)$$

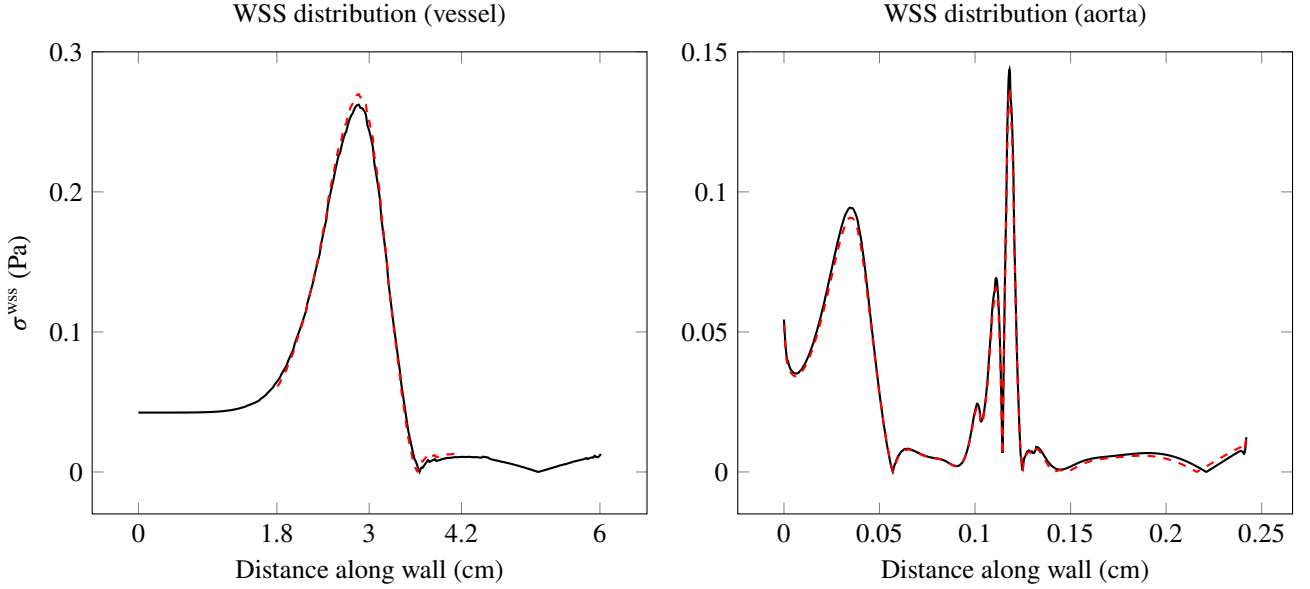


FIGURE 4 True wall shear stress distribution σ_h^{WSS} (—) and its reconstruction using simulation-based imaging $\sigma_H^{\text{WSS}}(\cdot, \mu^*)$ from MRI grids ($N = 9$ VPD for stenosis, $N = 10$ VPD for aorta) with a noise level of $\kappa = 20\%$ (---) along the intersection of the top wall of stenotic vessel (*left*) and bottom wall of the aorta (*right*) with the MRI domain, both at $\text{Re} = 1000$.

for $i = 1, \dots, N$. The weighting function for the i th voxel, $w_i : \Omega \rightarrow \mathbb{R}$, is the normalized tensor product of a sinc function with a smoothed box centered at (X_i, Y_i) , i.e.,

$$w_i : x \mapsto \bar{w}_i(x) \left(\int_{\Omega} \bar{w}_i dv \right)^{-1}, \quad \bar{w}_i : x \mapsto \Psi(x_1, X_i, \Delta x) \Psi(x_2, Y_i, \Delta y), \quad (8)$$

where the component-wise, non-normalized weighting function, $\Psi : \mathbb{R} \times \mathbb{R} \times \mathbb{R}_{>0} \rightarrow \mathbb{R}$, is defined as

$$\Psi : (s, c, \Delta s) \mapsto \text{sinc} \left(\frac{s-c}{\Delta s} \right) \chi(s, c, 4\Delta s). \quad (9)$$

The sinc function is included to mimic the point-spread function of MRI scanners that use a Fourier transform to map raw MRI data into flow velocities. The one-dimensional smoothed box function, $\chi : \mathbb{R} \times \mathbb{R} \times \mathbb{R}_{>0} \rightarrow \mathbb{R}$, is defined as

$$\chi : (s, s_0, \omega) \mapsto \frac{1}{1 + \exp(-(s - (s_0 - \omega/2))/\gamma))} - \frac{1}{1 + \exp(-(s - (s_0 + \omega/2))/\gamma))} \quad (10)$$

with center s_0 , width ω , and smoothness parameter γ . The smoothed box function localizes the integrand in (7) to the center of a particular voxel, allowing for some overlap between voxels, and ensures the integrand is sufficiently smooth for the integral to be well-approximated using numerical quadrature. Following the work in¹⁷, we take the smoothness parameter to be proportional to the voxel spacing, $\gamma = 0.1 \min\{\Delta x, \Delta y\}$. In this work, (6) is used to define the synthetic MRI data and define the SBI cost function (Section 2.3); a complete description of the approach can be found in¹⁷. Figures 2 and 3 show the synthetic MRI data ($N = 9$ VPD for stenosis, $N = 10$ VPD for aorta) extracted from the true flow with ($\kappa = 20\%$) and without noise for the stenosis and aorta test cases, respectively.

We use standard methods from the MRI literature to compute the WSS directly from the MRI data, $\sigma_N^{\text{WSS}}(x)$, at any point $x \in \partial\Omega_w$ ^{34,47}. First, we use the raw voxel velocity data v_h to compute a bilinear flow field reconstruction; we call this bilinear flow field v_N . Then, assuming no flow penetration through the walls, the tangential component of the surface traction in (5) can be written as

$$\tau = \mu(BB^T)\nabla v \cdot n, \quad (11)$$

where the columns of $B(x) \in \mathbb{R}^{d \times (d-1)}$ form a basis of the tangent space at $x \in \Omega_w$ (orthogonal complement of $n(x)$); see derivation in Appendix A. The normal gradient is computed using an approach similar to that in^{34,47}, i.e., construct a quadratic approximation of the velocity field in the normal direction from the bilinear flow field and assume the velocity is zero at x ,

because it performed favorably relative to several alternatives in a comparative study³⁴. The quadratic velocity along the outward normal n originating at the point x takes the form

$$\tilde{v}_N(\cdot; x, n) : \mathbb{R} \rightarrow \mathbb{R}^d, \quad \tilde{v}_N(\cdot; x, n) : r \mapsto v_N(x - \delta n)\psi_1(r) + v_N(x - 2\delta n)\psi_2(r) \quad (12)$$

where $\{\psi_0, \psi_1, \psi_2\}$ are one-dimensional quadratic Lagrangian polynomials associated with the nodes $\{0, \delta, 2\delta\}$, and $\delta \in \mathbb{R}_{>0}$ is the increment used to determine the points along the normal at which to fit the quadratic function to the bilinear flow field. In this work, we choose the increment to be proportional to the voxel spacing, $\delta = 1.2 \min\{\Delta x, \Delta y, 0.06\}$ (cm). Finally, the gradient of the velocity in the normal direction is approximated as $\tilde{v}'_N(0)$ and the tangential component of the surface traction (τ_N) and wall shear stress (σ_N^{wss}) at $x \in \Omega$ are computed as

$$\tau_N(x) = \mu(B(x)B(x)^T)\tilde{v}'_N(0; x, n(x)), \quad \sigma_N^{\text{wss}}(x) = \|\tau_N(x)\|. \quad (13)$$

This approach makes two unrealistic assumptions, namely, that the point on the boundary x and corresponding normal $n(x)$ are known exactly. In practice, these geometric properties must be approximated from scanned images, which introduces additional error that was quantified in³⁴. Since the position on the wall and the corresponding normal are known in the SBI setting, we use this information to maintain fairness in the comparison between MRI postprocessing and SBI.

2.3 | Simulation-based imaging

Simulation-based imaging aims to reconstruct a high-fidelity *in vivo* flow image from a CFD simulation that has been certified with MRI flow measurements. It optimally fits a CFD simulation to MRI flow data that can be noisy, sparse, and low-resolution by modifying the boundary conditions, material properties, and the initial condition. In this work, we adjust the inflow boundary conditions to fit the CFD simulation to the MRI data. That is, we consider the Navier-Stokes equation in (2) subject to the following boundary conditions

$$v = 0 \text{ on } \partial\Omega_w, \quad v = \hat{v}(\cdot; \mu) \text{ on } \partial\Omega_{\text{in}}, \quad \sigma \cdot n = 0 \text{ on } \partial\Omega_{\text{out}} \quad (14)$$

where $\hat{v} : \mathbb{R}^d \times \mathcal{D} \rightarrow \mathbb{R}^d$ is the parametrized inflow function, $\mu \in \mathcal{D}$ is a vector of parameters, and $\mathcal{D} \subset \mathbb{R}^d$ is the admissible parameter space. In this work, we take the inflow velocity to be parallel to the normal of the inflow boundary surface following¹⁷, which leads to

$$\hat{v} : (x; \mu) \mapsto \frac{(B_0 - x_2)(B_0 + x_2)}{B_0^2}(\mu, 0) \quad (15)$$

for the vessel case study, i.e., a parabolic profile for the x_1 velocity that is zero at the wall ($x_2 = \pm B_0$) with μ defining the peak of the parabola. A similar parabolic parametrization of the normal-directed inflow velocity is used for the aorta.

The CFD simulation underlying SBI discretizes the Navier-Stokes equation in (2) with the parametrized boundary conditions in (14) using the finite element method as described in Section 2.1; the corresponding velocity field is denoted $v_H(x; \mu)$. In the *in vivo* setting, the geometry of the flow domain is obtained by segmenting an angiogram scan from which a mesh is generated using standard tools^{48,49,50}. In this study, we directly generate a high-order mesh of the two geometries considered (Section 2.1).

The parameterized inflow boundary conditions are determined by optimally fitting the parameterized CFD solution to the MRI data

$$\mu^* = \arg \min_{\mu \in \mathcal{D}} I(\mu), \quad I : \mu \mapsto \sum_{i=1}^N \frac{\alpha_i}{2} \|\Xi_i(v_H(\cdot; \mu)) - \bar{v}_i\|_2^2, \quad (16)$$

where $\alpha_i = 1$ if the i th voxel at least partially within the domain and zero otherwise and $I : \mathcal{D} \rightarrow \mathbb{R}$ is the cost function that measures the misfit between the MRI data and its prediction from the CFD simulation. The optimization problem in (16) is solved using a quasi-Newton method globalized with a line search⁵¹ and gradients of the objective function are computed efficiently using the adjoint method. From the solution of the SBI optimization problem (μ^*), the reconstructed flow field is the CFD simulation at the optimal parameter configuration, i.e., $v_H(\cdot; \mu^*)$. From the SBI reconstructed flow, we calculate the corresponding WSS, denoted $\sigma_H^{\text{wss}}(\cdot; \mu^*)$, using (5) with the SBI state $v_H(\cdot; \mu^*)$. The necessary derivatives of the flow solution required in (5) are readily available from the finite element basis functions.

Figures 2 and 3 show the SBI reconstruction of the flow field and its representation in the MR data space for the stenosis and aorta test cases, respectively. Additionally, Figure 4 shows the WSS reconstruction using SBI for both test cases. From these figures, it is clear that even with a moderately refined MRI voxel mesh ($N = 9$ VPD for stenosis, $N = 10$ VPD for aorta) and high noise level ($\kappa = 20\%$), the SBI reconstruction provides a good approximation to the true velocity field and WSS distribution. We will study its sensitivity to these parameters in Section 3.

The same point-spread function (Ξ) used to define the MRI data is used to sample the CFD solution for matching to the MR flow data in the objective function. This assumes the numerical point-spread function (6) will exactly reproduce the point-spread function of the MRI scanner, which is not true in practice, which may introduce additional modeling error. However, in this work, we do not consider the sensitivity of SBI to the point-spread function, instead we focus on its performance with respect to Reynolds number, MRI resolution, and noise.

3 | RESULTS

In this section, we study the performance of MRI- and SBI-based wall shear stress reconstructions as a function of MRI noise level, resolution of the MRI voxel grid, Reynolds number, and resolution of the CFD mesh used for SBI reconstruction. Comprehensive studies for the ideal stenosis geometry are used to draw conclusions regarding the performance of MRI and SBI wall shear stress reconstruction; these conclusions are then verified for the more complex setting of flow through an idealized aorta using targeted studies.

In each of these studies, we will quantitatively compare the WSS distributions, i.e., $\sigma_H^{\text{wss}}(\cdot; \mu^*)$ (SBI) and σ_N^{wss} (MRI) to σ_h^{wss} (true WSS), along the curve $\Gamma \subset \partial\Omega_w$, where Γ is the intersection of the top (bottom) wall of the vessel (aorta) with the limits of the MRI domain (which does not span the entire domain for the stenotic vessel case). The error will be quantified using the relative L^2 norm, reported as percentages,

$$e_{\text{SBI}} = \frac{\sqrt{\int_{\Gamma} |\sigma_h^{\text{wss}}(x) - \sigma_H^{\text{wss}}(x; \mu^*)|^2 dS}}{\sqrt{\int_{\Gamma} |\sigma_h^{\text{wss}}(x)|^2 dS}}, \quad e_{\text{MRI}} = \frac{\sqrt{\int_{\Gamma} |\sigma_h^{\text{wss}}(x) - \sigma_N^{\text{wss}}(x)|^2 dS}}{\sqrt{\int_{\Gamma} |\sigma_h^{\text{wss}}(x)|^2 dS}}, \quad (17)$$

where $e_{\text{SBI}}, e_{\text{MRI}} \in \mathbb{R}_{\geq 0}$ are the SBI and MRI WSS distribution errors, respectively, and the integrals are computed using Gaussian quadrature.

3.1 | Impact of the CFD resolution

The CFD mesh resolution used for SBI impacts the computational cost of the method so we study the sensitivity of the SBI wall shear stress reconstruction to the resolution of the mesh. For this study, we vary the noise $\kappa \in \{0, 5, 10, 15, 20\}$ (%), Reynolds number $\text{Re} \in \{100, 500, 1000\}$, MRI grid resolution $N \in \{3, 9, 15, 28\}$ (VPD), and consider the three meshes of increasing resolution shown in Figure 5 ($N_e = 368, 766, 1590$ elements, respectively). The finest mesh ($N_e = 1590$) is used to compute the reference (“true”) flow and smoothly resolves all flow features, whereas the two coarser meshes ($N_e = 368$ and $N_e = 766$) lead to numerical artifacts in the stenosis, but contain two and four times fewer elements, respectively, and the corresponding CFD simulations require a fraction of the compute time.

First, we observe that the WSS reconstruction error using SBI decreases as the CFD mesh is refined (Figure 6), which holds for almost all Reynolds numbers, noise levels, and MRI voxel grids considered. The noise in the MRI data tends to degrade the accuracy of the WSS reconstruction; however, its influence diminishes as the MRI voxel grid is refined, i.e., there is very little difference in the $\kappa = 0\%$ and $\kappa = 20\%$ WSS reconstruction with $N = 28$ VPD MRI grid, whereas there is a substantial difference with $N = 3$ VPD. We note that for the finest mesh ($N_e = 1590$), the WSS reconstruction has a relatively weak dependence on the Reynolds number of the flow, whereas there is a significant dependence on Reynolds number for the coarser meshes, e.g., for the coarse mesh with $N = 3$ VPD and $\kappa = 10\%$, the WSS error is around 5% for $\text{Re} = 100$ and close to 15% for $\text{Re} = 1000$. Even in the cases with large error, the optimization problem underlying SBI drives the CFD simulation to a configuration that agrees reasonably well with the true WSS distribution given the limitations of the discretization (Figure 7).

Together these observations imply that an underresolved mesh can be used for the SBI reconstruction at the cost of increasing the sensitivity of the WSS reconstruction to Reynolds number and the MRI voxel grid. This is significant because it means the high computational cost of SBI can be reduced by using a coarse mesh without significant loss in WSS reconstruction accuracy, provided a sufficiently high-resolution MRI data set is used. Alternatively, it implies that a limited amount of MRI data can be used (e.g., from fast patient scans) provided the CFD mesh used for SBI reconstruction is relatively fine, which indicates an inherent trade-off between scan and reconstruction time when using SBI. In the remainder, we will fix the CFD mesh resolution at $N_e = 1590$ and focus on the impact of the remaining parameters (noise, Reynolds number, MRI resolution).

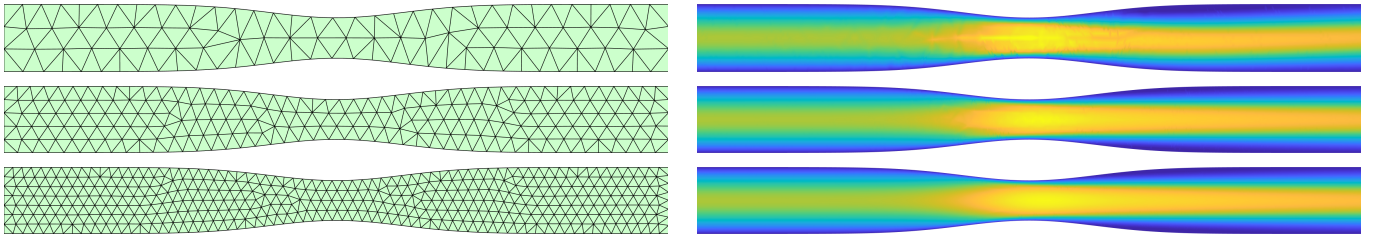


FIGURE 5 Meshes (*left*) of stenotic vessel used to study the sensitivity of SBI to resolution of the CFD mesh and the corresponding velocity field (*right*). Number of elements in mesh: $N_e = 368$ (*top row*), $N_e = 766$ (*middle row*), and $N_e = 1590$ (*bottom row*). Colorbar in Figure 2.

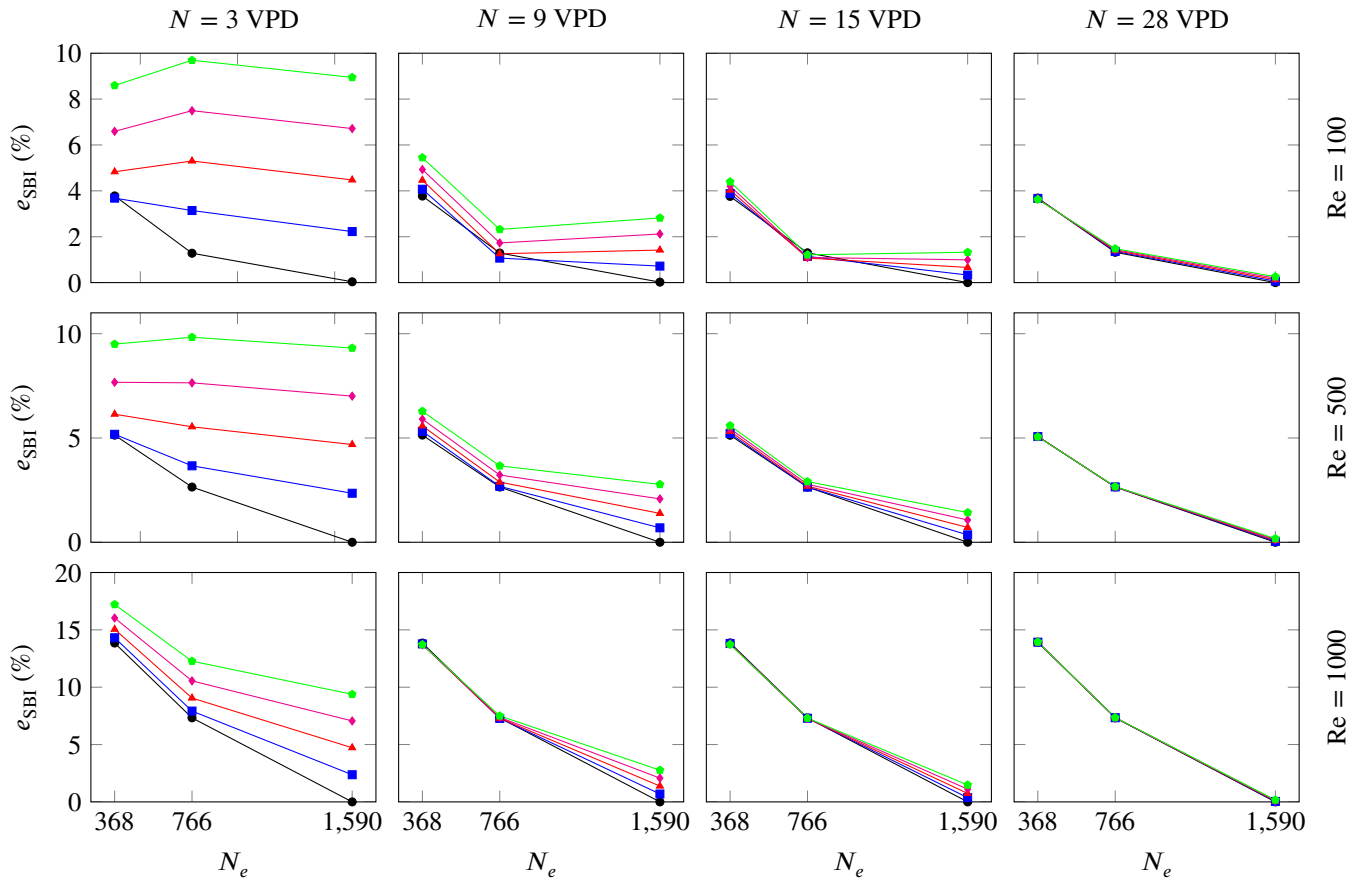


FIGURE 6 WSS reconstruction error using SBI as a function of CFD mesh resolution for various MRI grids (*columns*) and noise levels (*lines*) at Reynolds number 100 (*top row*), 500 (*middle row*), and 1000 (*bottom row*). Legend: $\kappa = 0\%$ ($\blackrightarrow\bullet$), $\kappa = 5\%$ ($\blackrightarrow\blacksquare$), $\kappa = 10\%$ ($\blackrightarrow\blacktriangle$), $\kappa = 15\%$ ($\blackrightarrow\blacktriangledown$), $\kappa = 20\%$ ($\blackrightarrow\blacklozenge$).

3.2 | Impact of noise, Reynolds number, and MRI resolution

In this section, we study the coupled effect that noise, Reynolds number, and the MRI voxel grid resolution have on the accuracy to which WSS is reconstructed using SBI (Section 2.3) and standard MRI reconstruction (Section 2.2). We vary the Reynolds number $\text{Re} \in \{100, 500, 1000\}$ because it is known to strongly impact the accuracy of WSS reconstructions based solely on MRI³⁴. We vary the noise $\kappa \in \{0, 5, 10, 15, 20\}$ (%) and MRI voxel grid $N \in \{3, 9, 15, 28\}$ (VPD) because these incorporate

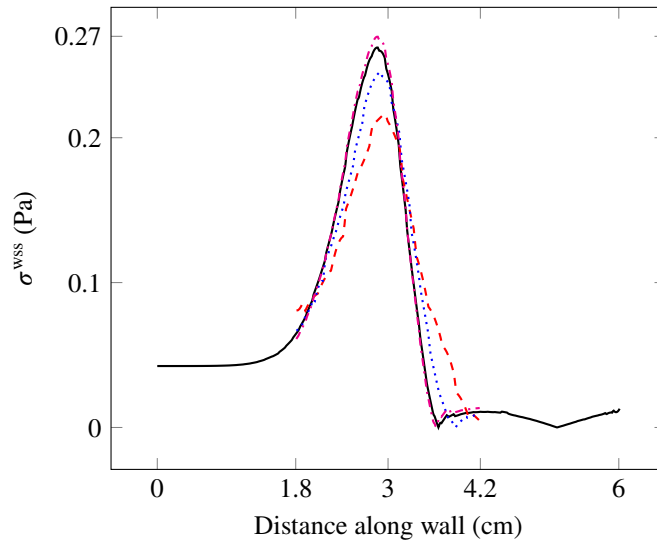


FIGURE 7 Wall shear stress distribution over intersection of top wall of stenotic vessel with MRI domain (Γ) using SBI with different mesh resolutions at Reynolds number $Re = 1000$, noise $\kappa = 20\%$, and MRI resolution $N = 9$ VPD (scenario in Figure 2). Legend: WSS distribution from true flow (—) and SBI WSS distribution using the mesh with $N_e = 368$ elements (---), $N_e = 766$ elements (·····), and $N_e = 1590$ elements (-·-·-); see Figure 5 for meshes.

extreme (best-case and worst-case) scenarios seen in practice; usually, for infant patients, noise levels are 3% – 10% and MRI resolution is 3 – 5 VPD^{43,44}. We use the CFD mesh with $N_e = 1590$ elements for SBI reconstruction.

First, we focus on the relationship between the WSS reconstruction error and resolution of the MRI voxel grid for various noise levels and Reynolds numbers (Figure 8). The error in the WSS reconstruction from MRI trends toward zero, albeit slowly, as the voxel grid is refined, which confirms the MRI WSS approach and implementation. Moreover, in the low noise setting, the WSS reconstruction error decreases toward a minimum (non-zero) value as the voxel grid is refined. However, for higher noise levels, additional MRI voxels can degrade the WSS reconstruction accuracy because it operates directly on the noisy MRI data and the length scale over which the noise (fixed magnitude of κ) varies decreases as the grid is refined, i.e., the noise varies more rapidly in the spatial domain. On the other hand, the WSS reconstruction from SBI is nearly exact in the no-noise setting and the error decreases monotonically as the voxel grid is refined for all Reynolds numbers and noise levels. While the overall error in the WSS reconstruction using SBI does increase with noise, additional MRI voxels do not limit or degrade the approximation as seen in the MRI-based reconstruction. This can be attributed to the fact that the WSS reconstruction using SBI does not *directly* operate on the noisy data; rather, the noisy data is used to reconstruct a noise-free CFD velocity field, which is used to compute the WSS. Therefore, the noise-sensitive operations, e.g., differentiation, are only applied to the noise-free SBI flow field, which leads to an approximation that is robust to noise in the MRI data. Finally, we observe that in the 3 – 5 VPD regime, the resolution commonly available for infant patients, the WSS reconstruction using SBI is significantly more accurate than using MRI alone. Even in the highest noise scenario ($\kappa = 20\%$), the SBI WSS reconstruction error is less than 10%, whereas the MRI WSS reconstruction error is about 50%.

Next, we investigate the relationship between the WSS reconstruction error and Reynolds number for various noise levels and MRI voxel grids (Figure 9). The accuracy of the WSS reconstruction directly from the MRI degrades as the Reynolds number increases, which agrees with other studies³⁴. The main exceptions come from configurations with high noise and many voxels per diameter where the error is already quite large (above 40%); in these cases, the WSS reconstruction error can decrease somewhat with increasing Reynolds number. On the other hand, WSS reconstruction from SBI is insensitive to Reynolds number, i.e., the range in the WSS reconstruction error is less than 1% from $Re = 100$ to $Re = 1000$ for all noise levels and decreases as the MRI grid is refined.

Next, we investigate the relationship between the WSS reconstruction error and noise level for various Reynolds numbers and MRI voxel grids (Figure 10). For the MRI-based WSS reconstruction, the error increases with noise except for the coarsest voxel grid ($N = 3$ VPD) where the error can slightly decrease as noise increases for higher Reynolds numbers (situations where the error is already quite large, at least 50%). As the MRI grid is refined, the rate at which the WSS error increases with respect to

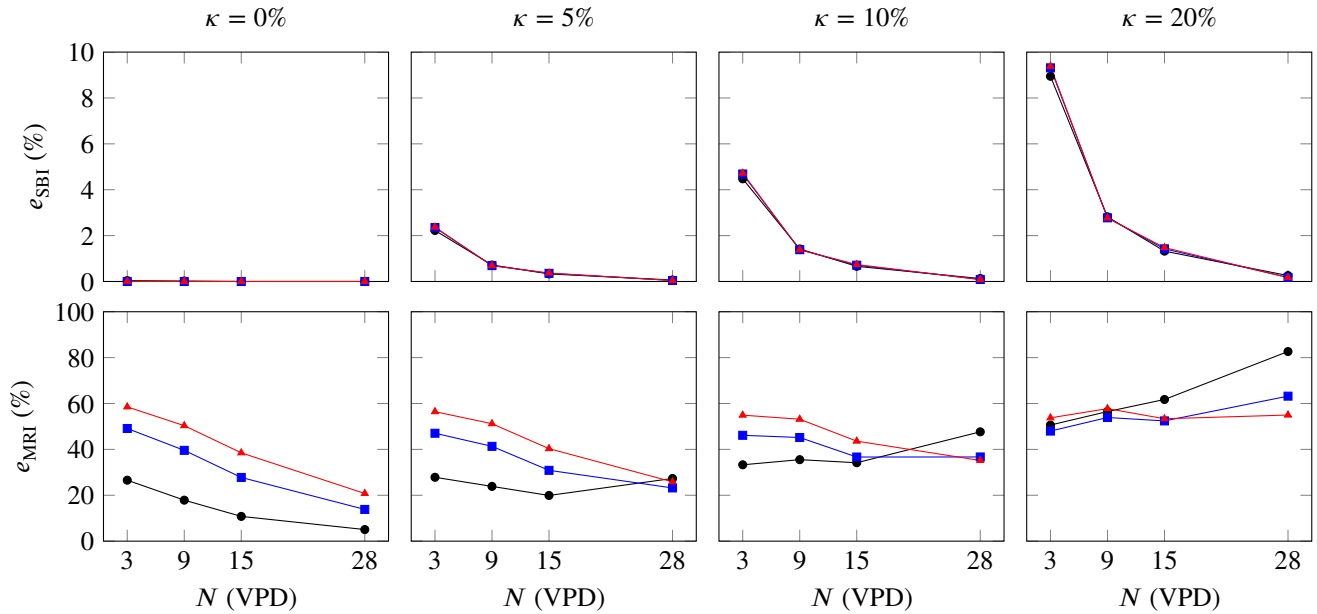


FIGURE 8 WSS reconstruction error using SBI (*top row*) and MRI (*bottom row*) as a function of MRI grid resolution for various noise levels (*columns*) and Reynolds numbers (*lines*). Legend: $Re = 100$ (\bullet), $Re = 500$ (\square), $Re = 1000$ (\triangle).

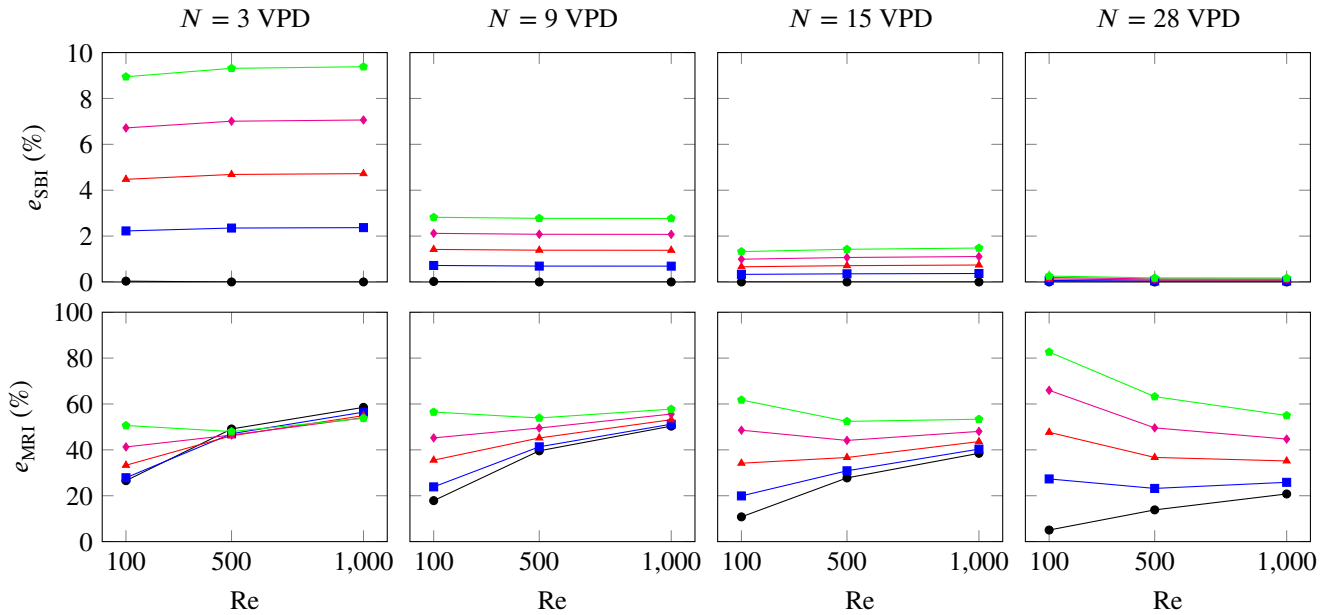


FIGURE 9 WSS reconstruction error using SBI (*top row*) and MRI (*bottom row*) as a function of Reynolds number for various MRI grid resolutions (*columns*) and noise levels (*lines*). Legend: $\kappa = 0\%$ (\bullet), $\kappa = 5\%$ (\square), $\kappa = 10\%$ (\triangle), $\kappa = 15\%$ (\diamond), $\kappa = 20\%$ (\circ).

noise accelerates due to the decreasing length scale over which the noise varies. The error in the WSS reconstruction using SBI increases linearly with the noise level with a decreasing slope as the MRI resolution increases (opposite of the trend observed with MRI-only WSS reconstruction). These observations hold across all Reynolds numbers considered $Re \in \{100, 500, 1000\}$.

To this point, we have aggregated the entire WSS distribution into a scalar to compare MRI- and SBI-based WSS reconstruction across numerous scenarios. We take a closer look at the entire WSS distribution as a scatter plot, whereby the actual value

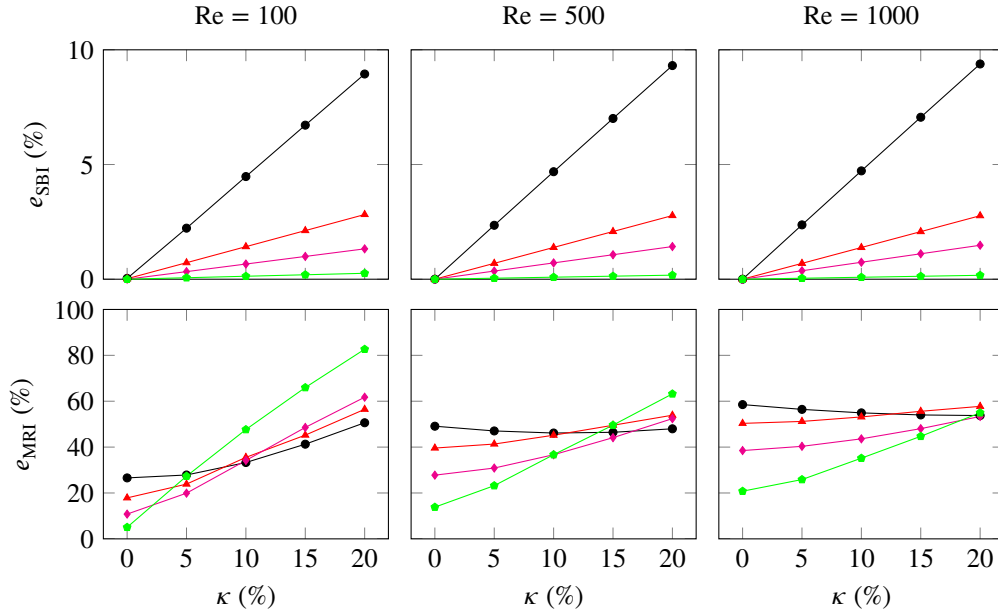


FIGURE 10 WSS reconstruction error using SBI (*top row*) and MRI (*bottom row*) as a function of noise level for various Reynolds numbers (*columns*) and MRI grid resolutions (*lines*). Legend: $N = 3$ VPD (—●—), $N = 9$ VPD (—▲—), $N = 15$ VPD (—◆—), $N = 28$ VPD (—■—).

of WSS is plotted against the reconstructed WSS for a number of points along the wall $x \in \Gamma$ (Figure 11); tight clustering around the line of identity implies the reconstruction is accurate and reliable. Because of the relatively weak dependence on Reynolds number (Figure 9), we fix $\text{Re} = 1000$ and vary the noise $\kappa \in \{5\%, 10\%, 15\%\}$ and MRI resolution $N \in \{9, 15, 28\}$ VPD. The SBI-based WSS reconstruction lies tightly clustered near the line of identity, whereas the MRI-based WSS reconstruction varies significantly from the line, particularly in the high-noise configurations.

3.3 | Verification with aorta geometry

A final set of numerical experiments was conducted using the coarctated aorta to demonstrate the key findings from the previous sections generalize to the more complex test case. To limit the parameter space to explore, we do not study the impact of mesh resolution on the SBI reconstruction. Furthermore, given the relative insensitivity of SBI to Reynolds number, we only consider a limited sampling of Reynolds numbers, i.e., $\text{Re} \in \{100, 1000\}$. We vary the noise $\kappa \in \{0, 5, 10, 20\}$ and MRI voxel grid $N \in \{3, 5, 10\}$ VPD; the finest MRI grid is restricted to $N = 10$ VPD (corresponds to 60×90 voxel grid) because the MRI domain covers a larger region compared to the stenotic vessel.

The relationship between the WSS reconstruction error and resolution of the MRI voxel grid for various noise levels and Reynolds numbers (Figure 12) is consistent with findings for the stenotic vessel. That is, the accuracy of the WSS reconstruction from MRI improves as the MRI voxel grid is refined for the low-noise settings, whereas it degrades in the higher noise settings. On the other hand, the WSS reconstruction error from SBI decreases as the MRI voxel grid is refined for all noise levels considered.

Similarly, the relationship between the WSS reconstruction error and noise for various Reynolds numbers and MRI voxel grids (Figure 13) is consistent with findings for the stenotic vessel. For MRI, the WSS reconstruction error increases rapidly when the noise exceeds $\kappa = 5\%$ and increases most rapidly for the finest MRI voxel grid. For SBI, the WSS reconstruction error increases linearly with the noise level with a slope that decreases as the MRI voxel grid is refined.

Overall, the results from the aorta test case agree with those from the vessel, particularly the trends with respect to variations in the MRI grid resolution and noise.

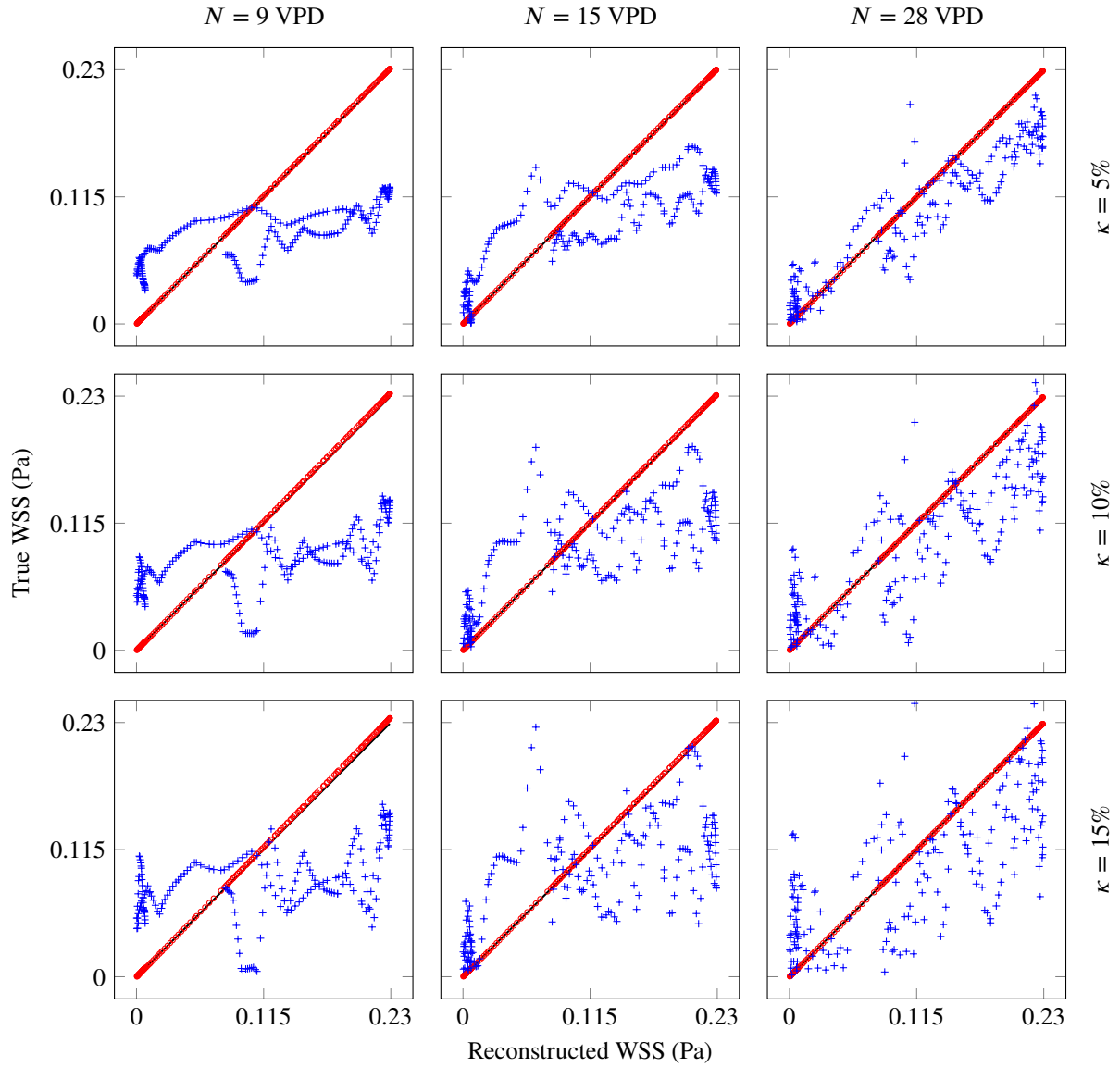


FIGURE 11 Scatter plot of the true WSS vs. the reconstructed WSS using SBI (\odot) and MRI ($+$) for 200 points along the upper wall intersected with the MRI domain (Γ). The rows correspond to noise levels $\kappa = 5\%$, 10% , 15% and the columns correspond to MRI resolutions $N = 9, 15, 28$ VPD. Tight clustering around the line of identity (—) indicates accurate WSS reconstruction along Γ .

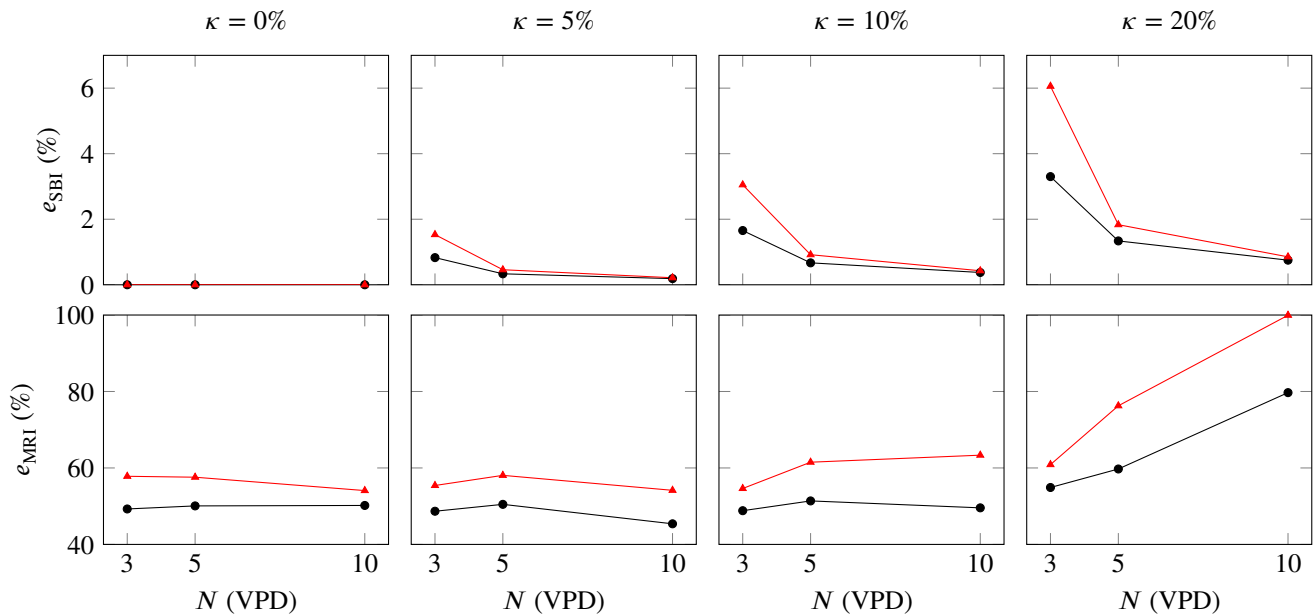


FIGURE 12 WSS reconstruction error using SBI (*top row*) and MRI (*bottom row*) as a function of MRI grid resolution for various noise levels (*columns*) and Reynolds numbers (*lines*) for coarctated aorta test case. Legend: $\text{Re} = 100$ (—●—), $\text{Re} = 1000$ (—▲—).

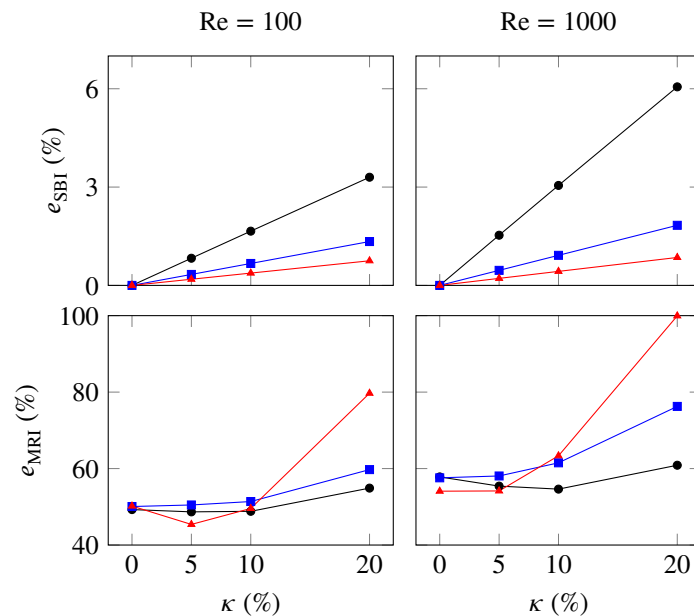


FIGURE 13 WSS reconstruction error using SBI (*top row*) and MRI (*bottom row*) as a function of noise level for various Reynolds numbers (*columns*) and MRI grid resolutions (*lines*). Legend: $N = 3$ VPD (—●—), $N = 5$ VPD (—■—), $N = 10$ VPD (—▲—).

4 | DISCUSSION

4.1 | Summary

This paper details a simulation-based imaging framework for blood flow imaging and WSS reconstruction based on using numerical optimization to fit a CFD simulation to MRI flow velocity data. The primary contribution of the paper are two synthetic test cases—flow through a stenotic vessel and coarctated aorta—that directly compare WSS reconstruction accuracy using SBI and standard MRI postprocessing techniques. We found the SBI method can accurately reconstruct WSS and is relatively insensitive to the resolution of the MRI data and Reynolds number of the flow. The WSS reconstruction error of SBI increases only linearly with noise in the MRI data with a slope that is inversely proportional to the resolution of the MRI data. Furthermore, coarser CFD grids can be used for the SBI reconstruction than used for the reference flow at the cost of increased sensitivity to the resolution of the MRI data and Reynolds number of the flow. On the other hand, WSS reconstruction from MRI data is less accurate than SBI and more sensitive to noise, resolution of the MRI data, and the Reynolds number of the flow.

4.2 | Conclusions

The wall shear stress reconstruction directly from MRI data showed sensitivity to the Reynolds number of the flow, the resolution of the MRI grid, and the noise in the MRI data. Without noise, the reconstructed WSS converged to the true WSS distribution as the MRI grid is refined; however, for higher noise levels the accuracy degrades as the MRI grid is refined. This can be attributed to the noise in the domain varying more rapidly, i.e., over a smaller length scale given by the MRI voxel spacing. Because the MRI WSS reconstruction fits a quadratic function to this noisy data, it is inherently sensitive to the length scale over which the noise varies. We also observed the accuracy of the WSS reconstruction directly from the MRI data degrades as the Reynolds number of the flow increases for most voxel grids and noise levels considered. Lastly, we found the error of the WSS reconstruction increases as the noise in the MRI data increases and grows faster as the MRI grid is refined. These findings are consistent with studies in the literature^{30,31,32,34,36}, which show that the accuracy of WSS computations directly from MRI data are limited by a fundamental trade-off between noise and resolution and become less reliable as the Reynolds number of the flow increases.

On the other hand, WSS reconstruction from SBI is relatively insensitive to the Reynolds number of the flow, the resolution of the MRI grid, and the noise in the MRI data. For all Reynolds numbers and noise levels considered, the WSS reconstruction accuracy improves as the MRI grid is refined. Furthermore, the reconstruction is reliable for all MRI grids considered, i.e., the largest WSS reconstruction error for the coarctated aorta test case was $e_{\text{SBI}} = 6\%$, which occurred at Reynolds number $Re = 1000$ with only $N = 3$ VPD and $\kappa = 20\%$ noise level. The accurate WSS reconstruction in the small data and high noise regime is attributed to the significant amount of *a priori* information leveraged by SBI including the geometry of the domain and governing equations (with unknown inflow boundary conditions) that are not exploited when reconstructing WSS from MRI data alone. Next, we observed that WSS reconstruction from SBI showed relatively little sensitivity to the Reynolds number of the flow over the limited range considered in this work. We expect these results to generalize throughout the laminar regime, but break down as the transitional and turbulent regimes are approached. Lastly, for all Reynolds numbers and MRI grids considered, the error in the WSS reconstruction using SBI increased linearly with noise; the maximum error observed is 10% for the stenotic vessel and 6% for the coarctated aorta which occur at a larger noise than usually observed in practice ($\kappa = 20\%$). This relatively minor sensitivity to noise is attributed to the fact that SBI does not directly compute WSS from a noisy field; rather, the noisy MRI data is used to reconstruct a noise-free CFD velocity field, which is then used to compute WSS. Because the velocity field reconstruction is reliable in the presence of zero-mean noise, the overall WSS reconstruction is reliable.

The SBI framework was shown to be moderately sensitive to the resolution of the mesh used for the SBI reconstruction. That is, a coarser mesh can be used for the SBI reconstruction than used to simulate the true flow; however, the sensitivity of the WSS reconstruction with respect to MRI resolution and Reynolds number increases. This provides an opportunity to reduce the computational cost of SBI for *in vivo* applications as it suggests there is some flexibility in designing the mesh used for SBI provided care is taken to ensure underresolution of the CFD velocity field is compensated with additional MRI resolution. Multi-fidelity optimization approaches that progressively refine inexpensive models, e.g., simulations on coarser meshes⁵² or reduced-order models⁵³, to accelerate convergence could be used to further reduce the cost of SBI. Alternatively, this observation implies that a limited amount of MRI data can be used (e.g., from fast patient scans) provided the CFD mesh used for SBI reconstruction is relatively fine due to the insensitivity of SBI to the quality/resolution of the MRI data in this scenario. This leads to an inherent trade-off between scan and reconstruction time when using SBI, which is fundamentally different and preferred than the trade-off between scan time and reconstruction quality attributed to traditional MRI postprocessing techniques.

4.3 | Limitations and future work

While this study resulted in a number of observations regarding the strengths and weaknesses of using SBI to reconstruct WSS, there are a number of limitations that offer promising paths for future research. First, a study of the impact of varying the point-spread function used in the SBI reconstruction from that used to compute the true flow would provide insight into the sensitivity of SBI for *in vivo* applications because the point-spread function of MRI scanners is not known with certainty, but can be modeled and estimated depending on the MRI protocol. Also, it would be interesting to include additional parameters to optimize in the SBI reconstruction, e.g., material properties of blood (with Newtonian or non-Newtonian fluid models) and outflow conditions, to further understand the ability of SBI to reconstruct a fully patient-specific flow. Finally, it is important to understand how the results obtained in this study generalize to scenarios closer to clinical applications, e.g., three-dimensional domains, unsteady flows, and higher Reynolds number flows.



APPENDIX

A SIMPLIFICATION OF TANGENTIAL COMPONENT OF WALL TRACTION

To derive the simplified expression for the tangential component of the wall traction in (11), we consider a point $x \in \partial\Omega_w$. All spatially varying quantities will be evaluated at this point; however, for brevity, the explicit dependence on x will be dropped. Let \mathcal{T} denote the $(d - 1)$ -dimensional tangent space of the wall $\partial\Omega_w$ at x , i.e., \mathcal{T} is a linear space such that for any $\xi \in \mathcal{T}$, $\xi \cdot n = 0$. In addition, let the columns of the matrix $B \in \mathbb{R}^{d \times (d-1)}$ be an orthogonal basis of \mathcal{T} , which implies

$$B^T n = 0, \quad B^T B = I_{d-1}. \quad (\text{A1})$$

From the no-slip condition ($v = 0$ on $\partial\Omega_w$), we have that for any $\xi \in \mathcal{T}$, $\nabla v \cdot \xi = 0$, which implies

$$\nabla v \cdot B = 0. \quad (\text{A2})$$

Next, we observe that the columns of $[B \ n]$ form a basis of \mathbb{R}^d and expand the traction vector at x in this basis

$$t = B t_s + n t_n, \quad (\text{A3})$$

where $t_s \in \mathbb{R}^{d-1}$ and $t_n \in \mathbb{R}$ are the coefficients of the traction vector expansion. From this expansion, the tangential component of the traction vector reduces to

$$\tau = (I - n n^T) t = B t_s, \quad (\text{A4})$$

where we used (A1) and unity of the normal vector n . Furthermore, by multiplying (A3) by B^T and using (A1), we have

$$t_s = B^T t. \quad (\text{A5})$$

Next, we substitute the expression for the traction in (5) into the above equation to yield

$$t_s = B^T [\mu(\nabla v + \nabla v^T)n + Pn] = \mu B^T (\nabla v \cdot n), \quad (\text{A6})$$

where we used (A1) and (A2). Finally, we combine (A4) and (A6) to yield the simplified expression for the tangential component of the wall traction in (11).

ACKNOWLEDGMENTS

The authors would like to thank Fritiof Hegardt for providing the aorta mesh and simulation. This material is based upon work supported by the Air Force Office of Scientific Research (AFOSR) under award number FA9550-20-1-0236 and the Swedish Research Council grant 2018-03721, the Crafoord Foundation, the Swedish strategic e-science research program eSENCE, and the Swedish Society of Medicine. The content of this publication does not necessarily reflect the position or policy of any of these supporters, and no official endorsement should be inferred.

References

1. Edelstein WA, Glover GH, Hardy CJ, Redington RW. The intrinsic signal-to-noise ratio in NMR imaging. *Magnetic Resonance in Medicine*. 1986;3(4):604–618.
2. Portnoy S, Kale SC, Feintuch A, Tardif C, Pike GB, Henkelman RM. Information content of SNR/resolution trade-offs in three-dimensional magnetic resonance imaging. *Medical Physics*. 2009;36(4):1442–1451.
3. Markl M, Schnell S, Wu C, et al. Advanced flow MRI: emerging techniques and applications. *Clinical Radiology*. 2016;71(8):779–795.
4. Holland DJ, Malioutov DM, Blake A, Sederman AJ, Gladden LF. Reducing data acquisition times in phase-encoded velocity imaging using compressed sensing. *Journal of Magnetic Resonance*. 2010;203(2):236–246.
5. Liu J, Dyverfeldt P, Acevedo-Bolton G, Hope M, Saloner D. Highly accelerated aortic 4D flow MR imaging with variable-density random undersampling. *Magnetic Resonance Imaging*. 2014;32(8):1012–1020.
6. Lustig M, Donoho D, Pauly JM. Sparse MRI: The application of compressed sensing for rapid MR imaging. *Magnetic Resonance in Medicine: An Official Journal of the International Society for Magnetic Resonance in Medicine*. 2007;58(6):1182–1195.
7. Tariq U, Hsiao A, Alley M, Zhang T, Lustig M, Vasanawala SS. Venous and arterial flow quantification are equally accurate and precise with parallel imaging compressed sensing 4D phase contrast MRI. *Journal of Magnetic Resonance Imaging*. 2013;37(6):1419–1426.
8. Lundervold AS, Lundervold A. An overview of deep learning in medical imaging focusing on MRI. *Zeitschrift für Medizinische Physik*. 2019;29(2):102–127.
9. Vishnevskiy V, Walheim J, Kozerke S. Deep variational network for rapid 4D flow MRI reconstruction. *Nature Machine Intelligence*. 2020;2(4):228–235.
10. Hoon N, Jalba A, Eisemann E, Vilanova A. Temporal interpolation of 4D PC-MRI blood-flow measurements using bidirectional physics-based fluid simulation.. In: :59–68; 2016; Bergen, Norway.
11. Hoon N, Pelt R, Jalba A, Vilanova A. 4D MRI flow coupled to physics-based fluid simulation for blood-flow visualization. In: :121–130; 2014.
12. Funke SW, Nordaas M, Evju O, Alnaes MS, Mardal KA. Variational data assimilation for transient blood flow simulations: Cerebral aneurysms as an illustrative example. *International Journal for Numerical Methods in Biomedical Engineering*. 2019;35(1):e3152.
13. Gaidzik D, Roloff C, Speck O, Thévenin D, Janiga G. Transient flow prediction in an idealized aneurysm geometry using data assimilation. *Computers in Biology and Medicine*. 2019;115:103507.
14. Goenezen S, Chivukula VK, Midgett M, Phan L, Rugonyi S. 4D subject-specific inverse modeling of the chick embryonic heart outflow tract hemodynamics. *Biomechanics and Modeling in Mechanobiology*. 2016;15(3):723–743.
15. Morbiducci U, Gallo D, Massai D, et al. Outflow conditions for image-based hemodynamic models of the carotid bifurcation: implications for indicators of abnormal flow. *Journal of Biomechanical Engineering*. 2010;132(091005).
16. Rispoli VC, Nielsen JF, Nayak K, Carvalho J. Using Fourier velocity encoded MRI data to guide CFD simulations. In: :584–587; 2015.
17. Töger J, Zahr MJ, Aristokleous N, Markenroth B K, Carlsson M, Persson PO. Blood flow imaging by optimal matching of computational fluid dynamics to 4D-flow data. *Magnetic Resonance in Medicine*. 2020;84(4):2231–2245.
18. Wood NB, Weston SJ, Kilner PJ, Gosman AD, Firmin DN. Combined MR imaging and CFD simulation of flow in the human descending aorta. *Journal of Magnetic Resonance Imaging: An Official Journal of the International Society for Magnetic Resonance in Medicine*. 2001;13(5):699–713.

19. Boussel L, Rayz V, McCulloch C, et al. Aneurysm growth occurs at region of low wall shear stress: patient-specific correlation of hemodynamics and growth in a longitudinal study. *Stroke*. 2008;39(11):2997–3002.
20. Cheng C, Tempel D, Van Haperen R, et al. Atherosclerotic lesion size and vulnerability are determined by patterns of fluid shear stress. *Circulation*. 2006;113(23):2744–2753.
21. Fedak PWM, Verma S, David TE, Leask RL, Weisel RD, Butany J. Clinical and pathophysiological implications of a bicuspid aortic valve. *Circulation*. 2002;106(8):900–904.
22. Frydrychowicz A, François CJ, Turski PA. Four-dimensional phase contrast magnetic resonance angiography: potential clinical applications. *European Journal of Radiology*. 2011;80(1):24–35.
23. Groen HC, Gijzen FJH, Van Der Lugt A, et al. High shear stress influences plaque vulnerability. *Netherlands Heart Journal*. 2008;16(8):280–283.
24. Lasheras JC. The biomechanics of arterial aneurysms. *Annual Review of Fluid Mechanics*. 2007;39:293–319.
25. Malek AM, Alper SL, Izumo S. Hemodynamic shear stress and its role in atherosclerosis. *Journal of the American Medical Association*. 1999;282(21):2035–2042.
26. Papaioannou TG, Stefanadis C. Vascular wall shear stress: basic principles and methods. *Hellenic Journal of Cardiology*. 2005;46(1):9–15.
27. Reneman RS, Arts T, Hoeks APG. Wall shear stress—an important determinant of endothelial cell function and structure—in the arterial system in vivo. *Journal of Vascular Research*. 2006;43(3):251–269.
28. Rosenthal E. Coarctation of the aorta from fetus to adult: curable condition or life long disease process?. *Heart*. 2005;91(11):1495–1502.
29. Shaaban AM, Duerinckx AJ. Wall shear stress and early atherosclerosis: a review. *American Journal of Roentgenology*. 2000;174(6):1657–1665.
30. Ooij P, Potters WV, Guédon JJ, et al. Wall shear stress estimated with phase contrast MRI in an in vitro and in vivo intracranial aneurysm. *Journal of Magnetic Resonance Imaging*. 2013;38(4):876–884.
31. Potters WV, Marquering HA, VanBavel E, Nederveen AJ. Measuring wall shear stress using velocity-encoded MRI. *Current Cardiovascular Imaging Reports*. 2014;7(4):9257.
32. Potters WV, Ooij P, Marquering H, vanBavel E, Nederveen AJ. Volumetric arterial wall shear stress calculation based on cine phase contrast MRI. *Journal of Magnetic Resonance Imaging*. 2015;41(2):505–516.
33. Cheng CP, Parker D, Taylor CA. Quantification of wall shear stress in large blood vessels using Lagrangian interpolation functions with cine phase-contrast magnetic resonance imaging. *Annals of Biomedical Engineering*. 2002;30(8):1020–1032.
34. Petersson S, Dyverfeldt P, Ebbers T. Assessment of the accuracy of MRI wall shear stress estimation using numerical simulations. *Journal of Magnetic Resonance Imaging*. 2012;36(1):128–138.
35. Sotelo J, Urbina J, Valverde I, et al. 3D quantification of wall shear stress and oscillatory shear index using a finite-element method in 3D CINE PC-MRI data of the thoracic aorta. *IEEE Transactions on Medical Imaging*. 2016;35(6):1475–1487.
36. Ha H, Kim GB, Kweon J, et al. Hemodynamic measurement using four-dimensional phase-contrast MRI: quantification of hemodynamic parameters and clinical applications. *Korean Journal of Radiology*. 2016;17(4):445–462.
37. Trudnowski RJ, Rico RC. Specific gravity of blood and plasma at 4 and 37 C. *Clinical Chemistry*. 1974;20(5):615–616.
38. Nader E, Skinner S, Romana M, et al. Blood rheology: key parameters, impact on blood flow, role in sickle cell disease and effects of exercise. *Frontiers in physiology*. 2019;10:1329.
39. Arzani A, Shadden SC. Characterizations and correlations of wall shear stress in aneurysmal flow. *Journal of Biomechanical Engineering*. 2016;138(1):014503.

40. Persson PO, Strang G. A simple mesh generator in MATLAB. *SIAM Review*. 2004;46(2):329–345.
41. Wolf RL, Ehman L, Riederer SJ, Rossman PJ. Analysis of systematic and random error in MR volumetric flow measurements. *Magnetic Resonance in Medicine*. 1993;30(1):82–91.
42. Garcia J, Van Der Palen RLF, Bollache E, et al. Distribution of blood flow velocity in the normal aorta: effect of age and gender. *Journal of Magnetic Resonance Imaging*. 2018;47(2):487–498.
43. Akturk Y, Ozbal Gunes S. Normal abdominal aorta diameter in infants, children and adolescents. *Pediatrics International*. 2018;60(5):455–460.
44. Cebal JR, Putman CM, Alley MT, Hope T, Bammer R, Calamante F. Hemodynamics in normal cerebral arteries: qualitative comparison of 4D phase-contrast magnetic resonance and image-based computational fluid dynamics. *Journal of Engineering Mathematics*. 2009;64(4):367–378.
45. Aja-Fernández S, Tristán-Vega A. A review on statistical noise models for magnetic resonance imaging. *LPI, ETSI Telecomunicacion, Universidad de Valladolid, Spain, Tech. Rep.* 2013;.
46. McGibney G, Smith MR. An unbiased signal-to-noise ratio measure for magnetic resonance images. *Medical Physics*. 1993;20(4):1077–1078.
47. Osinski JN, Ku DN, Mukundan Jr S, Loth F, Pettigrew RI. Determination of wall shear stress in the aorta with the use of MR phase velocity mapping. *Journal of Magnetic Resonance Imaging*. 1995;5(6):640–647.
48. Kang D, Woo J, Kuo CCJ, Slomka PJ, Dey D, Germano G. Heart chambers and whole heart segmentation techniques. *Journal of Electronic Imaging*. 2012;21(1):010901.
49. Prakosa A, Malamas P, Zhang S, et al. Methodology for image-based reconstruction of ventricular geometry for patient-specific modeling of cardiac electrophysiology. *Progress in Biophysics and Molecular Biology*. 2014;115(2-3):226–234.
50. Stanescu T, Jans HS, Wachowicz K, Fallone BG. Investigation of a 3D system distortion correction method for MR images. *Journal of Applied Clinical Medical Physics*. 2010;11(1):200–216.
51. Nocedal J, Wright S. *Numerical Optimization*. Springer Science & Business Media; 2006.
52. Ziems JC, Ulbrich S. Adaptive multilevel inexact SQP methods for PDE-constrained optimization. *SIAM Journal on Optimization*. 2011;21(1):1–40.
53. Zahr MJ, Farhat C. Progressive construction of a parametric reduced-order model for PDE-constrained optimization. *International Journal for Numerical Methods in Engineering*. 2015;102(5):1111–1135.